Effect of bulges on the stability of boundary layers

Ali H. Nayfeh, Saad A. Ragab, and Ayman A. AlMaaitah

Articles you may be interested in

Nonlinear stability of boundary layer solution to the Boltzmann equation with diffusive effect at the boundary
J. Math. Phys. **50**, 103303 (2009); 10.1063/1.3220562

Effect of a bulge on the subharmonic instability of boundary layers
Phys. Fluids A **2**, 937 (1990); 10.1063/1.857654

Boundary layer stability calculations
Phys. Fluids **30**, 3351 (1987); 10.1063/1.866467

Stability of a Stokes boundary layer
J. Acoust. Soc. Am. **81**, 861 (1987); 10.1121/1.394566

Stability of a Bulged Theta Pinch
Phys. Fluids **13**, 2735 (1970); 10.1063/1.1692858

Effect of bulges on the stability of boundary layers

Ali H. Nayfeh, Saad A. Ragab, and Ayman A. Al-Maaitah
Department of Engineering Science and Mechanics, Virginia Polytechnic Institute and State University, Blacksburg, Virginia 24061

The instability of flows around hump and dip imperfections is investigated. The mean flow is calculated using interacting boundary layers, thereby accounting for viscous/inviscid interaction and separation bubbles. Then, the two-dimensional linear stability of this flow is analyzed, and the amplification factors are computed. Results are obtained for several height/width ratios and locations. The theoretical results have been used to correlate the experimental results of Walker and Greening (British Aeronautical Research Council 5950, 1942). The observed transition locations are found to correspond to amplification factors varying between 7.4 and 10.0, consistent with previous results for flat plates. The method accounts for both viscous and shear-layer instabilities. Separation is found to increase significantly the amplification factor.

I. INTRODUCTION

The performance of natural laminar flow (NLF) airfoils is critically dependent on the location of transition, which may be strongly influenced by surface imperfections. Although modern metal and composite manufacturing techniques can provide smooth surfaces that are compatible with NLF, manufacturing tolerance criteria are needed for other unavoidable surface imperfections. These imperfections include waviness and bulges, steps and gaps at junctions, and three-dimensional roughness elements such as flush screw head slots and incorrectly installed flush rivets. Other unavoidable discontinuities arise from the installation of leading edge panels on wings, nacelles, and empennage surfaces and the installation of access panels, doors, and windows on fuselage noses and engine nacelles.[1-3] Because discontinuities cannot be avoided, a guide is needed for manufacturing tolerances. The mechanisms by which these imperfections cause transition include amplification of Tollmien–Schlichting waves, Kelvin–Helmholtz instability (for separated flows), amplification of cross-flow vorticity, Goertler instability, enhancement of receptivity of free-stream turbulence and acoustic disturbances, and any interaction between two or more of these mechanisms.[3-5]

Walker and Greening[6] made wind tunnel experiments to determine the effect of two-dimensional smooth bulges and hollows on the transition of the flow over a flat plate. They used surface tubes to determine the location of transition from laminar to turbulent flow. Their bulges and hollows were mounted on one side of a smooth flat aluminum plate, having an elliptic leading edge. Hislop[7] carried out similar experiments for narrow spanwise surface ridge corrugations on a flat plate. Walker and Cox[8] made wind tunnel experiments to study the effect of spanwise corrugations on an airfoil. These experiments were made for three forms of narrow corrugations (flat, arch, and wire) situated in the laminar boundary layer of a large symmetric airfoil (EQH 1260 section), mounted at zero angle of attack.

Fage[4] collected the three previous works[6-8] and established criteria for the critical heights of these imperfections that cause transition from laminar to turbulent flow. He found out that the flow conditions near a corrugation that affect transition are associated with a separation of the laminar boundary layer from its surface. Carmichael (e.g., Refs. 1 and 2) also developed empirically based criteria for allowable waviness and roughness that cause either laminar separation or amplification of Tollmien–Schlichting waves. His criteria are for allowable single and multiple bulges or sinusoidal waviness for both swept and unswept wing surfaces. His experiments include the influence of compressibility, suction, pressure gradients, multiple imperfections, and wing sweep. The flight experiments of Holmes, Obara, Martin, and Dormack[3] demonstrate the strong influence of some shapes of steps on the transition location and hence on the allowable heights of such imperfections. They found that by rounding a forward-facing step, the transition Reynolds number increases from 1800 to 2700. Carmichael's criteria are based on experimental results for waves located more than 25% chord downstream of the leading edge and hence they will underpredict allowable imperfections in the leading-edge region and overpredict allowable imperfections in regions of unaccelerated flows. Klebanoff and Tidstrom[9] used a spanwise trip wire as a roughness element, which causes local upstream and downstream separations, the latter extending 40–50 times the height of the wire before reattachment to the wall.

In spite of all these investigations, an understanding of the physics of the instability of flows around surface imperfections is still lacking. As a first step toward such an understanding, this work investigates the influence of a two-dimensional hump or dip on the two-dimensional stability. This work uses a combination of linear stability theory and the exp(N) criterion that has proven to be a valuable tool for correlating transition and for evaluating natural laminar flow as well as laminar flow control concepts. Since linear stability of parallel as well as nonparallel incompressible and compressible flows is well established, the major task in evaluating the influence of imperfections is an accurate prediction of the mean flow.

For smooth surfaces, one can use a conventional bound-

ary-layer formulation to solve for the mean flow over swept and unswept wing surfaces. However, conventional boundary-layer formulations cannot predict flow over surfaces with imperfections, such as suction strips and slots, waviness and bulges, steps and gaps at junctions, and three-dimensional roughness elements because of the strong viscous/inviscid coupling and flow separation. Instead, one needs to use a triple-deck formulation, an interacting boundary-layer formulation, or a Navier–Stokes solver. All these approaches account for the viscous/inviscid interaction as well as separation bubbles, but Navier–Stokes solvers are very expensive compared with triple-deck and interacting boundary-layer formulations. In this work, we use an interacting boundary-layer formulation, which already had been used to compute compressible as well as incompressible flows over smoothed steps, wavy surfaces and humps, convex and concave corners, suction or blowing slots, and finite-angle trailing edges. In most of these applications separation bubbles and upstream influence exist and comparisons with solutions of the Navier–Stokes equations and/or experiments had shown good agreement. Gleyzes, Cousteix, and Bonnet,[10] Vatsa and Carter,[11] and Davis and Carter[12] used interacting boundary-layer theory to analyze separation bubbles near the leading edges of airfoils. Davis, Carter, and Reshotko[13] developed an interacting boundary-layer technique for the calculation of transitional separation bubbles over infinite swept wings; the results are in good agreement with Horton's[14] detailed experimental data for separated flow over a swept plate.

The purpose of this work is to study the effect of a two-dimensional surface waviness, represented by a hump or a dip, on the two-dimensional stability of boundary layers over flat plates. Quartic humps with different sizes and locations are studied first. Then, the theory is used to correlate the experimental data of Walker and Greening.[6]

II. MEAN FLOW

The two-dimensional incompressible laminar boundary layer over the plate and the hump is determined by solving the interacting boundary-layer equations.[15,16] These equations account for upstream influence through the interaction of the viscous flow with the inviscid flow outside the boundary layer. Moreover, they are also capable of capturing separation bubbles without difficulties. Solutions are obtained by using a finite-difference method in which the grid spacings acknowledge the scalings predicted by the triple-deck theory in the interaction region.

Figures 1 and 2 show a small symmetric hump of height h^* and width $2b^*$ whose center is located at x'_m. We introduce dimensionless variables using L^* and U'_∞, where L^* is the distance from the leading edge to a reference point, as reference quantities. In terms of dimensionless variables, the hump shape is given by

$$y = y^*/L^* = (h^*/L^*) f(\zeta) , \qquad (1)$$

where

$$\zeta = (x^* - x_m^*)/b^* = (x - x_m)/b . \qquad (2)$$
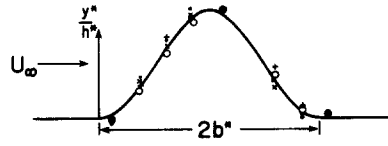
We present numerical results for a quartic hump given by

FIG. 1. The experimental hump shape. $\cdot$:$h^* = 0.061$ in., $\times$:$h^* = 0.052$ in., $\bigcirc$:$h^* = 0.036$ in., $+$:$h^* = 0.022$ in., —:calculated shape of hump.

$$f(\zeta) = \begin{cases} (1 - \zeta^2)^2 , & \text{if } |\zeta| \leqslant 1 , \\ 0 , & \text{if } |\zeta| > 1 , \end{cases} \qquad (3)$$

and the Walker and Greening hump

$$f(\zeta) = \begin{cases} 1 - 3\zeta^2 + 2|\zeta|^3 , & \text{if } |\zeta| \leqslant 1 , \\ 0 , & \text{if } |\zeta| > +1 . \end{cases} \qquad (4)$$

The flow field over the plate with the hump is assumed to be governed by the steady, incompressible boundary-layer equations

$$u \frac{\partial u}{\partial x} + v \frac{\partial u}{\partial y} = u_e \frac{du_e}{dx} + \frac{1}{Re} \frac{\partial^2 u}{\partial y^2} , \qquad (5)$$

$$\frac{\partial u}{\partial x} + \frac{\partial v}{\partial y} = 0 , \qquad (6)$$

where u_e is the streamwise edge velocity and

$$Re = U_\infty^* L^*/\nu^* . \qquad (7)$$

The no-slip and no-penetration conditions demand that

$$u = v = 0 \quad \text{at} \quad y = hf[\zeta(x)] . \qquad (8)$$

Away from the wall,

$$u \to u_e \quad \text{as} \quad y \to \infty . \qquad (9)$$

To solve Eqs. (5)–(9), we first use the Prandtl transposition theorem, let

$$z = y - hf[\zeta(x)] , \quad w = v - hu \frac{df}{dx} [\zeta(x)] \qquad (10)$$

and rewrite the problem as

$$u \frac{\partial u}{\partial x} + w \frac{\partial u}{\partial z} = u_e \frac{du_e}{dx} + \frac{1}{Re} \frac{\partial^2 u}{\partial z^2} , \qquad (11)$$

$$\frac{\partial u}{\partial x} + \frac{\partial w}{\partial z} = 0 , \qquad (12)$$

$$u = w = 0 \quad \text{at} \quad z = 0 , \qquad (13)$$

$$u \to u_e \quad \text{as} \quad z \to \infty . \qquad (14)$$

Then, we introduce the Levy–Lees variables specialized for incompressible flow

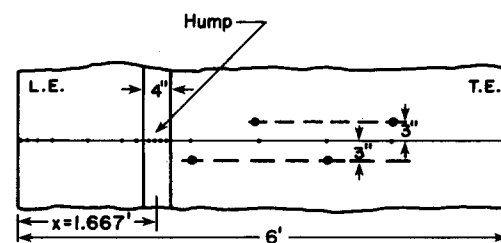$$\xi = \int_0^x u_e \, dx , \quad \eta = zu_e \sqrt{\frac{Re}{2\xi}} , \qquad (15)$$

FIG. 2. The configuration tested by Walker and Greening.[6] $\bullet$:Surface tube, $\cdot$:Static pressure tube.

$$F = \frac{u}{u_e}, \quad V = \frac{2\xi}{u_e}\left(F\frac{\partial \eta}{\partial x} + w\sqrt{\frac{\mathrm{Re}}{2\xi}}\right) \tag{16}$$

and rewrite Eqs. (11)–(14) as

$$2\xi F F_\xi + V F_\eta + \beta(F^2 - 1) - F_{\eta\eta} = 0, \tag{17}$$

$$2\xi F_\xi + V_\eta + F = 0, \tag{18}$$

$$F = V = 0 \quad \text{at } \eta = 0, \tag{19}$$

$$F \to 1 \quad \text{as } \eta \to \infty, \tag{20}$$

$$F = F(\xi_0, \eta) \quad \text{at } \xi = \xi_0, \tag{21}$$

where ξ_0 corresponds to a location upstream of the interaction region and

$$\beta = \frac{2\xi}{u_e}\frac{du_e}{d\xi}. \tag{22}$$

For smooth surfaces, one can use conventional boundary-layer calculations to determine the flow field. However, in the presence of the hump, one needs to account for the viscous/inviscid interaction. The interaction law relates the edge velocity u_e to the displacement surface

$$\delta = \frac{\sqrt{2\xi}}{u_e}\int_0^\infty (1 - F)\, d\eta. \tag{23}$$

Using thin airfoil theory,[17] we have

$$u_e = \tilde{u}_e + \frac{1}{\pi}\int_{\mathrm{L.E.}}^\infty \frac{(d/dt)(\tilde{u}_e \delta\, \mathrm{Re}^{-1/2})}{x - t}\, dt, \tag{24}$$

where $\tilde{u}_e$ is the inviscid surface velocity in the absence of the boundary layer that is also given by thin airfoil theory as

$$\tilde{u}_e = 1 + \frac{1}{\pi}\int_{\mathrm{L.E.}}^\infty \frac{dhf/dt}{x - t}\, dt, \tag{25}$$

where L.E. stands for the leading edge of the plate and f is defined in Eqs. (3) and (4). The principal values of the Cauchy integrals in Eqs. (24) and (25) are assumed. If we let $T = \bar{f} + \tilde{u}_e \delta$, where $\bar{f} = \sqrt{\mathrm{Re}}\, hf$, then Eq. (24) can be rewritten as

$$u_e = 1 + \frac{1}{\pi\sqrt{\mathrm{Re}}}\int_{\mathrm{L.E.}}^\infty \frac{dT/dt}{x - t}\, dt. \tag{26}$$

Equations (17)–(21) can be either solved simultaneously with the interaction law (26) or by iterating on (26). The latter approach suffers from convergence problems. Veldman[18] was the first to use the first approach. He integrated Eq. (26) by parts to obtain a second derivative for T and expressed u_e as a linear combination of the values of δ at the nodes. Davis and Werle[15] modified this approach by performing the integration by parts to eliminate the derivative of T and assumed T to be constant over a differencing interval. This yielded a first-order accurate scheme. In this paper, we follow Davis and Werle but assume T to vary linearly over a differencing interval, thereby yielding a second-order accurate scheme that is consistent with the accuracy of the differencing scheme employed for Eqs. (17) and (18).

We divide the x axis into equally spaced intervals of length Δx and let x_i denote the node points at which the boundary-layer solution is to be found. Following Davis and Werle, we let

$$\delta = c_1 \sqrt{x} \quad \text{for } 0 \leqslant x \leqslant x_l, \quad \delta = c_2\sqrt{x} \quad \text{for } x_r \leqslant x \leqslant \infty,$$

where x_l and x_r are the locations of the left and right boundaries of the interaction region. The constants c_1 and c_2 are determined by patching with the displacement thicknesses at $x_l + \frac{1}{2}\Delta x$ and $x_r - \frac{1}{2}\Delta x$. Taking x_i to be the center of an element extending from $x_i - \frac{1}{2}\Delta x$ to $x_i + \frac{1}{2}\Delta x$, Davis and Werle assumed that T is uniform over this element with a value equal to its central value T_i. This approximation is consistent with the first-order x differencing used by Davis and Werle. In the present paper, we use a second-order finite-difference scheme in solving the boundary-layer equations, therefore, we have to upgrade the accuracy of evaluating the Cauchy integral. We assume that T varies linearly over an element centered at x_i as

$$T = T_i + \frac{1}{2}(T_{i+1} - T_{i-1})\tau, \quad \text{for } |\tau| \leqslant \frac{1}{2}, \tag{27}$$

where

$$\tau = (x - x_i)/\Delta x. \tag{28}$$

Before substituting the linear expressions for T, we split the integral in Eq. (26) as

$$I \equiv \int_{\mathrm{L.E.}}^\infty \frac{dT/dt}{x - t}\, dt$$

$$= \lim_{\epsilon_1 \to 0}\left(\int_{\mathrm{L.E.}}^{x_l} + \int_{x_l}^{x-\epsilon_1} + \int_{x+\epsilon_1}^{x_r} + \int_{x_r}^\infty\right)\frac{dT/dt}{x - t}\, dt. \tag{29}$$

Integrating the second and third integrals by parts yields

$$I = \left(\int_{\mathrm{L.E.}}^{x_l} + \int_{x_r}^\infty\right)\frac{dT/dt}{x - t}\, dt + \frac{T(x_r)}{x - x_r} - \frac{T(x_l)}{x - x_l}$$

$$+ \lim_{\epsilon_1 \to 0}\left(\frac{T(x - \epsilon_1) + T(x + \epsilon_1)}{\epsilon_1}\right.$$

$$\left. - \int_{x_l}^{x-\epsilon_1}\frac{T\, dt}{(x - t)^2} - \int_{x+\epsilon_1}^{x_r}\frac{T\, dt}{(x - t)^2}\right). \tag{30}$$

Now, substituting the linear expressions for T and performing the indicated integrations and limits, we obtain

$$u_e(x_i) = 1 + \lambda\left\{\frac{\Delta x}{4}\left[\frac{T_1}{2x_l\sqrt{\xi_l\xi_i}}\ln\left(\frac{\sqrt{\xi_i} + 1}{\sqrt{\xi_i} - 1}\right)\right.\right.$$

$$+ \frac{T_m}{2x_r\sqrt{\xi_m\xi_i}}\ln\left(\frac{1 - \sqrt{\xi_i}}{1 + \sqrt{\xi_i}}\right)$$

$$\left. + \frac{T_m}{\sqrt{x_m x_r}}\frac{1}{\xi_i - 1} - \frac{T_1}{\sqrt{x_1 x_l}}\frac{1}{\xi_i - 1}\right]$$

$$\left. + \sum_{j=1}^m D_k T_j + \sum_{\substack{j=1 \\ j \neq i}}^m E_k(T_{j+1} - T_{j-1})\right\}, \tag{31}$$

where $k = |i - j|$, $D_k = (1 - 4k^2)^{-1}$,

$$E_k = \frac{1}{2}kD_k - \frac{1}{8}\ln\left[(2k - 1)/(2k + 1)\right],$$

$$\xi_i = \frac{x_i}{x_l}, \quad \zeta_i = \frac{x_i}{x_r}, \quad \lambda = \frac{4\,\mathrm{Re}^{-1/2}}{\pi\,\Delta x}.$$

We note that the terms in the square bracket in Eq. (31) are the contributions of the displacement thickness outside the interaction region, the second term is the contribution of the mean values of T at the centers of the intervals, and the last

term is the contribution of the slopes of T at the centers of the intervals. We note also that the second term is the dominant one in Eq. (31). It follows from Fig. 1 that x_l and x_r are given by

$$x_l = x_1 - \tfrac{1}{2}\Delta x, \quad x_r = x_m + \tfrac{1}{2}\Delta x,$$

where x_1 and x_m are the first and last node points in the interaction region. For later use, we rewrite Eq. (31) in the form

$$u_e(x_i) = \lambda G_i + \lambda\Gamma(\tilde{u}_e\delta)_i, \tag{32}$$

where

$$G_i = 1/\lambda + \tilde{u}_{ei} + (\tilde{u}_e\delta)_1 g_1^i + (\tilde{u}_e\delta)_m g_2^i$$
$$+ \sum_{\substack{j=1 \\ j\neq i}}^{m} D_k(\tilde{u}_e\delta)_j + E_k[(\tilde{u}_e\delta)_{j+1} - (\tilde{u}_e\delta)_{j-1}],$$
$$\text{if } 2 \leqslant i \leqslant m-1, \tag{33a}$$

$$G_1 = 1/\lambda + \tilde{u}_e + (\tilde{u}_e\delta)_m g_2^1 + D_1(\tilde{u}_e\delta)_2 - E_1(\tilde{u}\delta)_3$$
$$+ \sum_{j=3}^{m} D_k(\tilde{u}_e\delta)_j + E_k[(\tilde{u}_e\delta)_{j+1} - (\tilde{u}_e\delta)_{j-1}], \tag{33b}$$

$$G_m = 1/\lambda + \tilde{u}_{em} + (\tilde{u}_e\delta)_1 g_1^m$$
$$+ D_1(\tilde{u}_e\delta)_{m-1} - E_1(\tilde{u}_e\delta)_{m-2}$$
$$+ \sum_{j=1}^{m-2} D_k(\tilde{u}_e\delta)_j + E_k[(\tilde{u}_e\delta)_{j+1} - (\tilde{u}_e\delta)_{j-1}], \tag{33c}$$

$$\Gamma = 1, \quad \text{if } 2 \leqslant i \leqslant m-1, \tag{33d}$$
$$\Gamma = 1 + g_1^1 + E_1, \quad \text{for } i = 1, \tag{33e}$$
$$\Gamma = 1 + g_2^m + E_1, \quad \text{for } i = m, \tag{33f}$$
$$\tilde{u}_{ei} = \sum_{j=1}^{m} D_k \overline{f}_j + E_k(\overline{f}_{j+1} - \overline{f}_{j-1}). \tag{33g}$$

The definitions of the g's are apparent from Eq. (31).

Using three-point backward differencing, we obtain from Eqs. (18), (22), (23), and (31) the following form for the interaction law:

$$V_N + \phi\beta_i = \psi, \tag{34}$$

where

$$\phi = (\sqrt{2\xi_i}/\lambda\Gamma) a_0\tilde{u}_{ei}/(2\xi_i a_0 - \beta_i), \tag{35a}$$

$$\psi = -\eta_N + \sqrt{2\xi_i}\, a_0$$
$$\times\left(\frac{\alpha}{\lambda\Gamma} - \frac{G_i}{\Gamma} + \frac{a_1}{a_0}(u_e\delta)_{i-1} + \frac{a_2}{a_0}(u_e\delta)_{i-2}\right), \tag{35b}$$

$$\alpha = -\frac{u_{ei}\beta_i + 2\xi_i(a_1 u_{ei-1} + a_2 u_{ei-2})}{2\xi_i a_0 - \beta_i}, \tag{35c}$$

$$a_0 = \frac{1}{\xi_i - \xi_{i-1}} + \frac{1}{\xi_i - \xi_{i-2}}, \tag{35d}$$

$$a_1 = \frac{\xi_i - \xi_{i-2}}{(\xi_i - \xi_{i-1})(\xi_{i-1} - \xi_{i-2})}, \tag{35e}$$

$$a_2 = \frac{\xi_i - \xi_{i-1}}{(\xi_i - \xi_{i-2})(\xi_{i-1} - \xi_{i-2})}. \tag{35f}$$

Equations (17)–(21) and interaction law (34) are solved simultaneously using central differencing in the η direction and three-point backward differencing in the ξ direction. The flow upstream of the interaction region is assumed to be a Blasius flow.

III. STABILITY ANALYSIS

In this paper, we consider the two-dimensional spatial quasiparallel stability of the basic state determined by the interacting boundary-layer code. Since we are interested in correlating our results with the experimental transition results of Walker and Greening, we need to calculate the maximum growth rates and amplification factors and apply the results at finite Reynolds numbers. Thus we are interested in the unsteady solutions of the linearized Navier–Stokes equations for finite values of the Reynolds number and we are not interested in their asymptotic solutions as $\mathrm{Re}\to\infty$. In fact, the dimensionless frequencies involved are between 20×10^{-6} and 50×10^{-6}. The Reynolds numbers Re involved are less than 10^6, leading to the perturbation parameter $\epsilon = \mathrm{Re}^{-1/8}$, used in triple-deck theory, being greater than 0.18. Consequently, the asymptotic limit as $\mathrm{Re}\to\infty$ ($\epsilon\to0$), predicted by triple-deck theory for the lower branch of the neutral stability curve of the Blasius flow[19] is irrelevant to our problem. Therefore, we follow classical stability theory and introduce dimensionless quantities using the length scale $\delta_r = (\nu x_r^*/U_\infty^*)^{1/2}$. Although the use of this length scale has been justified for conventional aerodynamic surfaces, one might question the validity of its use for the configuration under investigation. It is justified a posteriori (see Sec. IV C). The calculated wavelengths for the geometrical and flow parameters for our configuration are the order of the boundary-layer thickness. Moreover, the results calculated using this model correlate the experimental transition data of Walker and Greening. Using this length scale leads to the classical quasiparallel stability equations. The nonparallel effects can be accounted for using the method of multiple scales,[20,21] which is the subject of a forthcoming paper.

We superimpose on the basic flow a two-dimensional unsteady disturbance. Thus we let

$$\tilde{u}(x,y,t) = U(x,y) + u(x,y,t), \tag{36a}$$
$$\tilde{v}(x,y,t) = 0 + v(x,y,t), \tag{36b}$$
$$\tilde{p}(x,y,t) = P(x) + p(x,y,t), \tag{36c}$$

where $U(x,y)$ and $P(x)$ are the basic streamwise velocity and pressure, respectively. Substituting Eqs. (36) into the Navier–Stokes equations, subtracting the basic-flow quantities, and linearizing the resulting equations, we obtain

$$\frac{\partial u}{\partial t} + U\frac{\partial u}{\partial x} + v\frac{\partial U}{\partial y} + \frac{\partial p}{\partial x} - \frac{1}{R}\nabla^2 u = 0, \tag{37}$$

$$\frac{\partial v}{\partial t} + U\frac{\partial v}{\partial x} + \frac{\partial p}{\partial y} - \frac{1}{R}\nabla^2 v = 0, \tag{38}$$

$$\frac{\partial u}{\partial x} + \frac{\partial v}{\partial y} = 0, \tag{39}$$

where $R = U_\infty^* \delta_r/\nu$. The no-slip and no-penetration conditions at the wall yield

$$u = v = 0 \quad \text{at } y = hf(x) . \tag{40}$$

The vanishing of the disturbance away from the wall yields

$$u,v,p \to 0 \quad \text{as } y \to \infty . \tag{41}$$

We use the Prandtl–transposition theorem as in Eq. (10) and rewrite Eqs. (37)–(41) as

$$\frac{\partial u}{\partial t} + U\frac{\partial u}{\partial x} + w\frac{\partial U}{\partial z} + \frac{\partial p}{\partial x} - \frac{1}{R}\left(\frac{\partial^2 u}{\partial x^2} + \frac{\partial^2 u}{\partial z^2}\right) = 0 , \tag{42}$$

$$\frac{\partial w}{\partial t} + U\frac{\partial w}{\partial x} + \frac{\partial p}{\partial z} - \frac{1}{R}\left(\frac{\partial^2 w}{\partial x^2} + \frac{\partial^2 w}{\partial z^2}\right) = 0 , \tag{43}$$

$$\frac{\partial u}{\partial x} + \frac{\partial w}{\partial z} = 0 , \tag{44}$$

$$u = w = 0 \quad \text{at } z = 0 , \tag{45}$$

$$u, p, w \to 0 \quad \text{as } z \to \infty . \tag{46}$$

In deriving Eqs. (42)–(44) from Eqs. (37)–(39), we have assumed the quasiparallel assumption and neglected terms of $O(\epsilon^2)$, where $\epsilon^8 = \text{Re}$, except the terms $R^{-1}\nabla^2 u$ and $R^{-1}\nabla^2 w$ that are needed to resolve the critical layer.

We seek a solution for Eqs. (42)–(46) in the form of a two-dimensional traveling wave as

$$(u,w,p) = [\tilde{u}(z),\tilde{w}(z),\tilde{p}(z)]\exp\left[i\left(\int \alpha \, dx - \omega t\right)\right] , \tag{47}$$

where α is the wavenumber and ω is the frequency of the disturbance. For temporal stability, α is real and ω is complex; its real part represents the frequency whereas its imaginary part represents the growth rate. For spatial stability, ω is real and α is complex. In this paper, we consider the spatial stability case in which α is complex.

Substituting Eqs. (47) into Eqs. (42)–(46), we separate the x and t variations and obtain the eigenvalue problem

$$i(\alpha U - \omega)\tilde{u} + \tilde{w}D\tilde{U} + i\alpha\tilde{p} - (1/R)(D^2 - \alpha^2)\tilde{u} = 0 , \tag{48}$$

$$i(\alpha U - \omega)\tilde{w} + D\tilde{p} - (1/R)(D^2 - \alpha^2)\tilde{w} = 0 , \tag{49}$$

$$i\alpha\tilde{u} + D\tilde{w} = 0 , \tag{50}$$

$$\tilde{u} = \tilde{w} = 0 \quad \text{at } z = 0 , \tag{51}$$

$$\tilde{u},\tilde{w},\tilde{p} \to 0 \quad \text{as } z \to \infty , \tag{52}$$

where $D = d/dz$. To solve this eigenvalue problem, we express Eqs. (48)–(50) as a system of first-order ordinary differential equations and determine its solution numerically using a combination of Suport[22] and a Newton–Raphson procedure. For a given U, ω, and R, we determine α and then calculate the N factor from

$$N = -\int_{x_0}^{x} \alpha_i \, dx = -2\int_{R_0}^{R} \alpha_i \, dR , \tag{53}$$

where R_0 is the Reynolds number corresponding to branch I of the neutral stability curve.

IV. RESULTS AND DISCUSSION

A. The mean-flow characteristics

The mean flow over humps was computed for different height/width ratios and different hump locations. Figure 3 shows the skin-friction coefficient
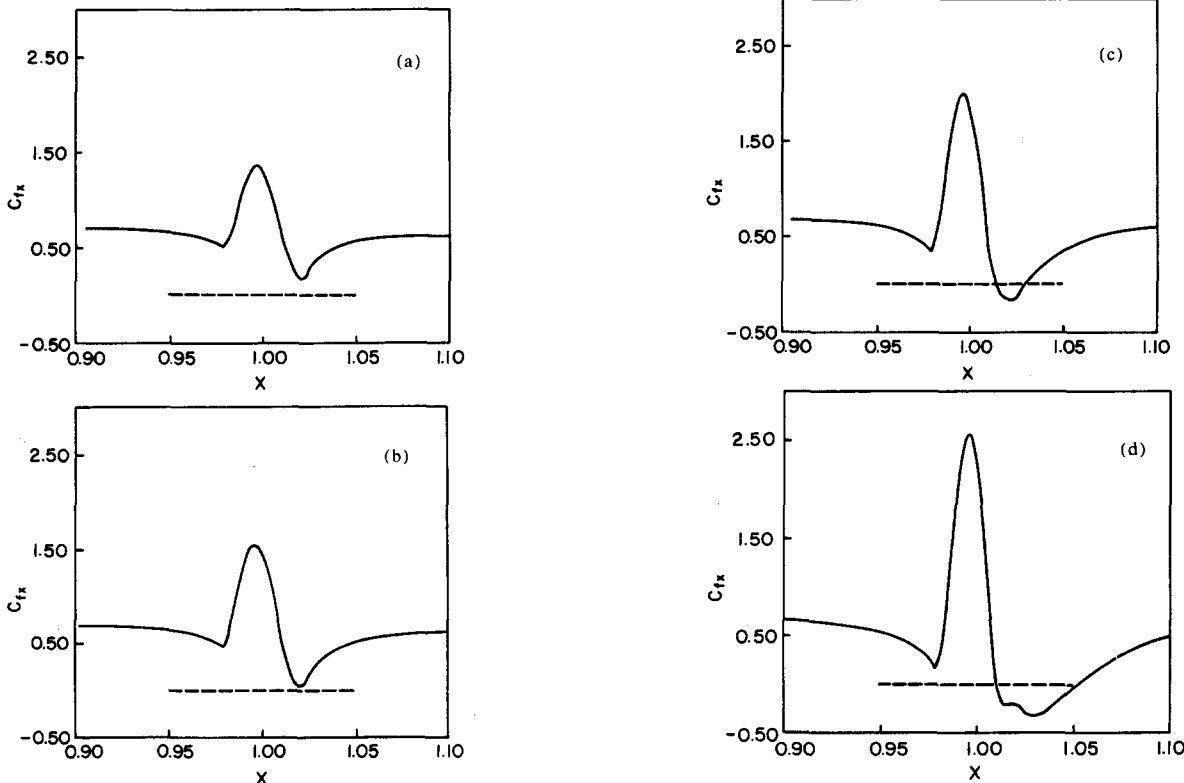

FIG. 3. The effect of the hump height on the skin-friction distribution when $x_m^*/L^* = 1.0$ ($R = 975$): (a) $h^*/b^* = 0.019$; (b) $h^*/b^* = 0.024$; (c) $h^*/b^* = 0.037$; and (d) $h^*/b^* = 0.055$.
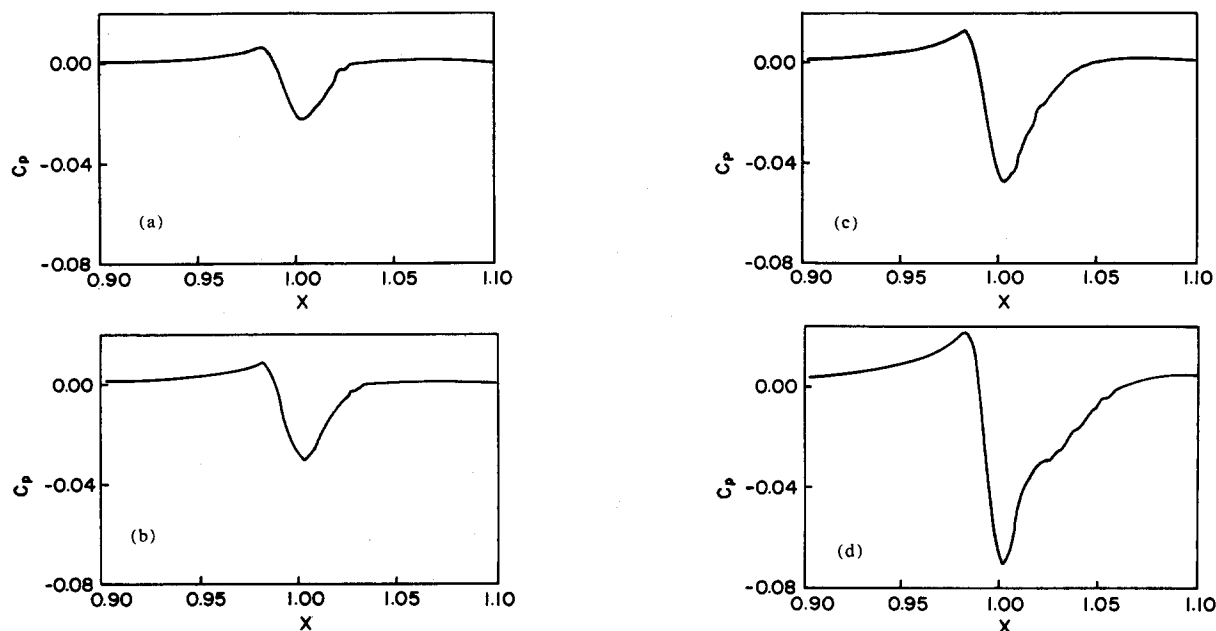
FIG. 4. The effect of the hump height on the surface pressure distribution when $x_m^*/L^* = 1.0$ ($R = 975$): (a) $h^*/b^* = 0.019$; (b) $h^*/b^* = 0.024$; (c) $h^*/b^* = 0.037$; and (d) $h^*/b^* = 0.055$.

$$c_f \sqrt{\text{Re}_\infty} = \frac{2U_e^2}{\sqrt{2\xi}} \left.\frac{\partial F}{\partial \eta}\right|_{\eta=0}$$

for a quartic hump of various heights placed at $x_m^*/L^* = 1.0$ ($R = 975$), where L^* is the location corresponding to $\text{Re} = 9.5 \times 10^5$ at the middle of the hump. The interactive solution matches with the Blasius flow both upstream and far downstream of the hump. However, the upstream influence of the hump is weaker than the downstream influence. In fact, the upstream influence decays exponentially while the downstream influence decays algebraically as shown by Smith[23] for small humps. The corresponding pressure distributions are shown in Fig. 4. For $h^*/b^* \leqslant 0.024$ the flow is attached. As h^*/b^* increases beyond 0.024, a separation bubble forms at the leeside of the hump. The size of the bubble increases as h^*/b^* increases. For height/width ratios $O(1)$, one would expect a breakaway separation for which

the present interacting boundary-layer model breaks down, and one needs to use a Navier–Stokes solver.

We note that the small wiggles in the mean flow quantities are due to the coarse streamwise grid. Refining the streamwise grid eliminates these wiggles.[24]

Tables I and II show some of the mean-flow properties for the humps and dips of Walker and Greening. The velocity u outside the boundary layer for the undistorted surface varies from 15.9 m/sec (53.0 ft/sec) to 28.5 m/sec (95.0 ft/sec) for the humps, and from 18.57 m/sec (61.9 ft/sec) to 25.47 m/sec (84.9 ft/sec) for the dips. The maximum transverse dimension h^* varies from 0.75 mm (0.03 in.) to 1.75 mm (0.07 in.) for the humps and from 1.425 mm (0.057 in.) to 1.675 mm (0.067 in.) for the dips. The observed transition length is denoted by L_T; it is measured from the leading edge to the observed transition location. The Reynolds numbers at the middle of the humps or dips R_m and at the transition location R_T are based on the reference length δ^* so that

TABLE I. Hump configurations in the experiments of Walker and Greening.[6]

Number	u ft/sec	h in.	L_T ft	h^*/b^*	R_m	R_T	Bubble size ΔR
1	82.6	0.031	4.58	0.0155	812	1346	00.0
2	69.4	0.0525	4.58	0.0263	830	1376	18.0
3	70.4	0.0555	4.58	0.0278	860	1426	29.6
4	53.0	0.0620	4.58	0.0310	744	1234	25.7
5	56.2	0.0665	4.58	0.0332	764	1267	28.8
6	53.8	0.0700	4.58	0.0350	753	1249	36.1
7	78.0	0.0530	3.75	0.0265	904	1357	26.9
8	76.0	0.0555	3.75	0.0278	892	1337	32.5
9	61.5	0.0620	3.75	0.0310	803	1205	31.6
10	62.4	0.0630	3.75	0.0315	810	1215	34.5
11	55.5	0.0680	3.75	0.0340	761	1142	34.6
12	95.0	0.0525	2.92	0.0263	997	1319	32.6
13	70.0	0.0620	2.92	0.0310	860	1138	32.8
14	92.4	0.0620	2.08	0.0310	983	1098	49.9

Number	u ft/sec	h in.	L_T ft	$h*/b*$	R_m	R_T	Bubble size ΔR
1	76.4	−0.057	4.58	0.0285	894	1483	37.7
2	65.8	−0.067	4.58	0.0335	831	1377	41.6
3	82.7	−0.057	3.75	0.0285	930	1395	39.8
4	61.9	−0.067	3.75	0.0335	807	1210	36.5
5	84.9	−0.057	2.92	0.0285	943	1248	41.3
6	69.7	−0.067	2.92	0.0285	855	1132	39.0

$$R_m = (\text{Re})^{1/2}, \quad R_T = [(L_T/L*)\text{Re}]^{1/2}. \qquad (54)$$

All of the previous quantities were calculated directly from the experimental data given by Walker and Greening,[6] but the streamwise extents of the separation bubbles are expressed as the difference in the Reynolds numbers at separation and reattachment; that is, $\Delta R = R(\text{reattachment}) - R(\text{separation})$ and ΔR is calculated using the interacting boundary-layer code. Except for hump No. 1 all the humps and dips in Tables I and II have separation bubbles.

Figure 5 shows the skin-friction and pressure-distribution coefficients for hump No. 14. One can see that the separation bubble occurs after the center of the hump. Figure 6 shows the variation of the streamwise velocity profiles for hump No. 14. The first and the last velocity profiles are at locations away from the hump; they are essentially Blasius profiles.
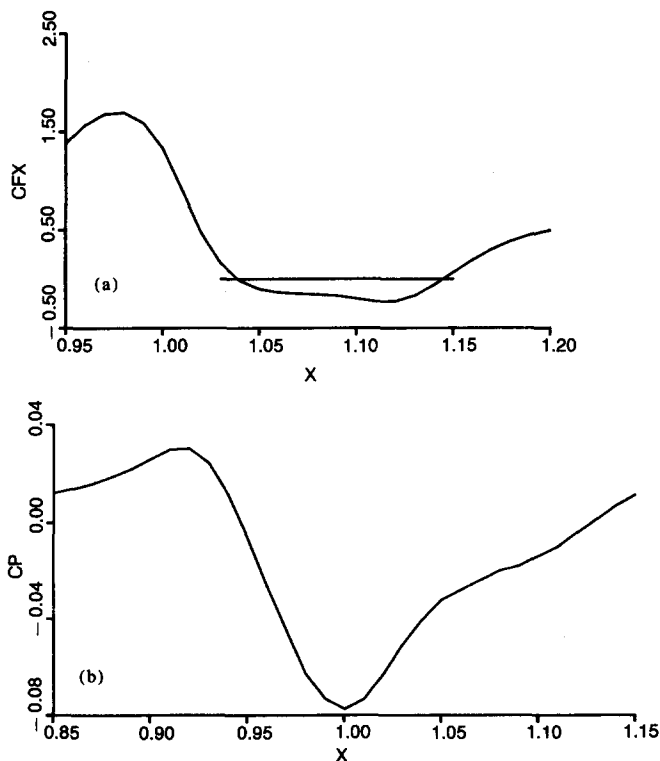

FIG. 5. Here are the skin-friction and pressure distributions for hump No. 14 in Table I. The hump is centered at $x_m^*/L* = 1.0 = 1.0$ ($R = 983$), $h*/b* = 0.031$.

B. Stability characteristics

First, we consider a quartic hump and study the effects of height/width ratio and hump location on the growth rates and the N factors of two-dimensional waves for the dimensionless frequency $F = \omega^* v^*/U^{*2} = 25 \times 10^{-6}$, which is the most dangerous frequency for the Blasius flow.

To investigate the influence of the height of a hump having a fixed width on the growth rates and N factors, we locate the center of the hump x_m^* at $L*$ corresponding to $R = 975$. The growth rates for $h*/b* = 0.019, 0.024, 0.037$, and 0.055 are depicted in Fig. 7. Shown also is the growth rate of the Blasius flow at the same frequency. The presence of the hump increases the growth rate in the interval $(x_i^*, x_m^* - b*)$, decreases the growth rate in the interval $(x_m^* - b*, x_m^*)$, and increases the growth rate again in the interval (x_m^*, x_r^*). The stabilizing and destabilizing effects are consistent with the gradients of the pressure distributions shown in Fig. 4.

Figure 8 shows the variation of the amplification factor with streamwise position for different heights of the hump. It shows that for humps with $h*/b* \lesssim 0.024$ for which the flow is attached, the humps have a negligible effect on the N factor. When $h*/b* = 0.037$, there is a small separation bubble, and the hump has a significant effect on the N factor. As $h*/b*$ increases further, the separation bubble increases, and the N factor increases.

Table III shows the variation of the maximum N factor at $F = 25 \times 10^{-6}$ with $h*/b*$. When $h*/b* = 0.037$ and 0.055, the maximum N factors are 11.02 and 12.67, respectively, compared with 9.84 for the Blasius flow. The Reynolds number $R = R_9$ at which N is 9 decreases from 1792 for
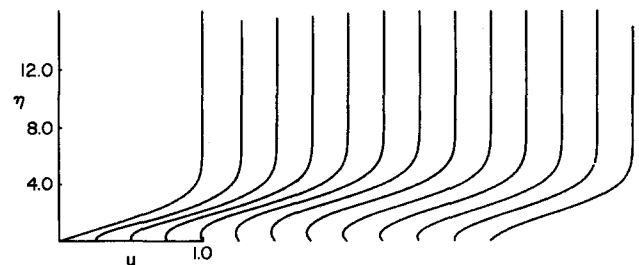

FIG. 6. The variation of streamwise velocity profiles along the plate for hump No. 14 in Table I. The hump is centered at $x_m^*/L* = 1.0$ ($R = 983$), $h*/b* = 0.031, b*/L* = 0.1$. The profiles correspond to the following values of R starting from left to right: 695, 1006, 1011, 1015, 1019, 1023, 1027, 1031, 1036, 1040, 1044, 1048, and 1052.
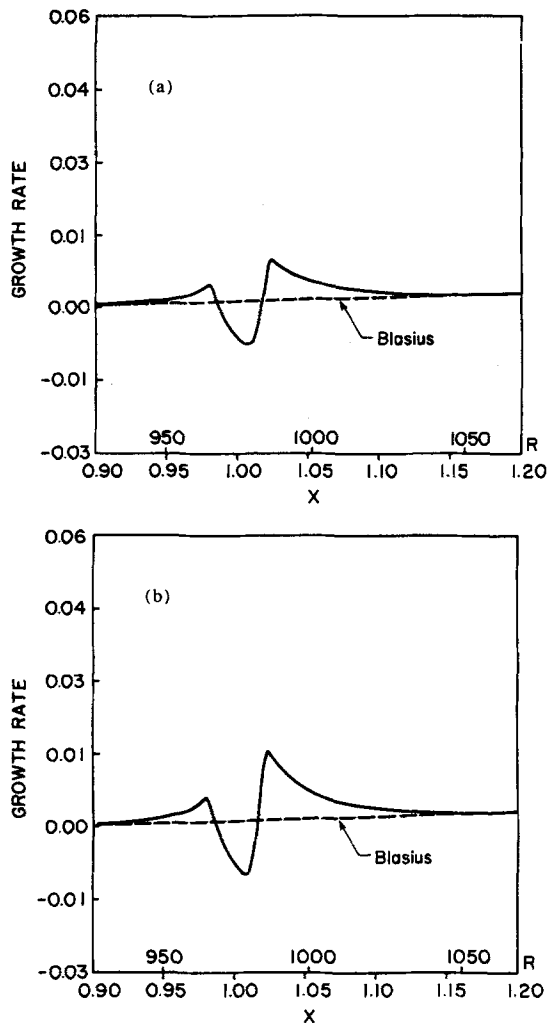
FIG. 7. The effect of the hump height on the streamwise distribution of the growth rate for $F = 25 \times 10^{-6}$. The flow conditions are the same as in Fig. 3: (a) $h^*/b^* = 0.019$; (b) $h^*/b^* = 0.024$; (c) $h^*/b^* = 0.037$; and (d) $h^*/b^* = 0.055$.

the Blasius flow to 1680 and 1552 for humps having $h^*/b^* = 0.037$ and 0.055, respectively.

Figure 9 shows the influence of the location of a hump having an $h^*/b^* = 0.055$ on the variation of the amplification factor at $F = 25 \times 10^{-6}$ with streamwise location. For
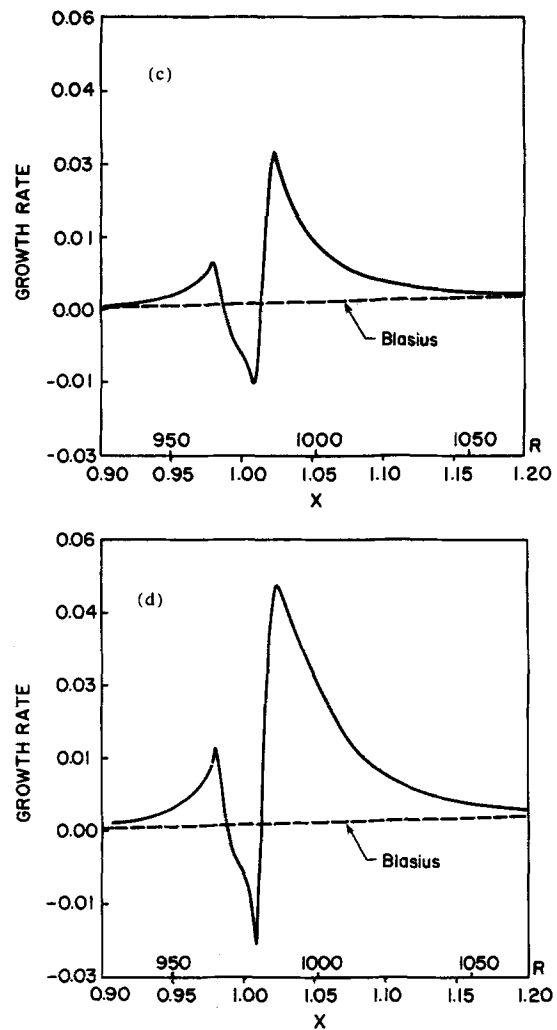
all locations at or upstream of branch I of the Blasius flow, the N factor increases to 3 in a short distance, namely, the interaction region of the hump. Downstream of the interaction region, the growth rates are practically the same as

FIG. 8. The effect of the hump height on the streamwise variation of the amplification factor $F = 25 \times 10^{-6}$. The flow conditions are the same as in Fig. 3: $h^*/b^* = $ (a) 0.019; (b) 0.024; (c) 0.037; (d) 0.055; and (e) Blasius.
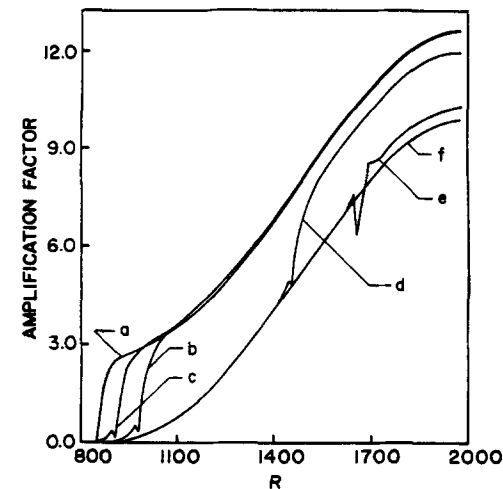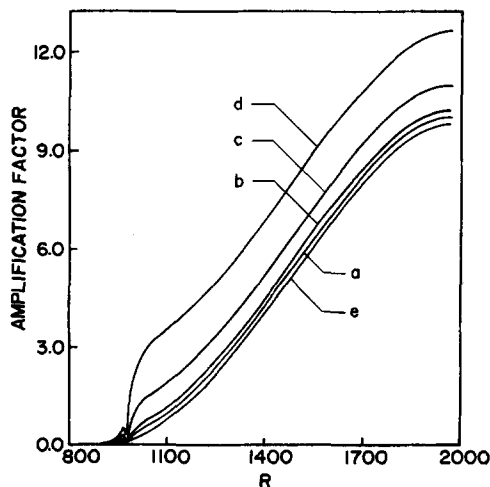

FIG. 9. The effect of the hump location on the streamwise variation of the amplification factor $F = 25 \times 10^{-6}$. The flow conditions are the same as in Fig. 5: $x_m^*/L^* = $ (a) 0.75; (b) 0.861; (c) 1.0; (d) 2.19; (e) 2.86; and (f) Blasius.

TABLE III. Variation of the maximum N-factor and the location at which $N = 9$ with the height of a quartic hump of half-width $b*/L_m^* = 2.274 \times 10^{-2}$ ($b*/\delta = 4.430$) whose center is at $R_m = 975$, $\delta = 5(\nu L*/U_\infty^*)^{1/2}$.

$h*/L*$	$h*/\delta$	$h*/b*$	R_9	N_{max}	Bubble length ΔR
0	0	0	1792	9.84	0
4.198×10^{-4}	0.082	0.019	1779	10.04	0
5.457×10^{-4}	0.106	0.024	1750	10.25	0
8.395×10^{-4}	0.164	0.037	1680	11.02	6.7
12.593×10^{-4}	0.246	0.055	1552	12.67	22.1

TABLE IV. Influence of the location of a quartic hump on the maximum N factor and the Reynolds number at which $N = 9$, $h*/b* = 0.0554$, $h*/L_m^* = 12.593 \times 10^{-4}$, L_m^* corresponds to $R = 975$, $\delta = 5(\nu L*/U_\infty^*)^{1/2}$.

R at center of hump	$h*/\delta$	R_9	N_{max}	Bubble length ΔR
844	0.284	1552	12.59	57.1
904	0.265	1552	12.68	23.5
975	0.246	1552	12.67	22.1
1443	0.166	1605	11.97	10.1
1648	0.145	1752	10.23	8.3

TABLE V. Variation of Reynolds number R_9 at which the computed N factor is equal to 9 and the computed N factor at the measured transition location with frequency for hump No. 5.

$F \times 10^6$	R_9	N_T
25.0	1513	5.7
30.0	1393	7.3
35.0	1315	8.4
37.5	1290	8.7
40.0	1306	8.5
45.0	$\cdots$	8.4

TABLE VI. Correlation of the theoretical and experimental results for the transition location for the humps in Table I.

Hump #	$h*$ in.	$h*/b*$	R_m	Separation bubble ΔR	R_T	N_T	$F_T \times 10^6$
1	0.0310	0.0155	812	00.0	1346	10.03	20.0
2	0.0525	0.0262	830	18.0	1376	8.20	37.5
3	0.0555	0.0278	860	29.6	1426	9.09	35.0
4	0.062	0.0319	744	25.7	1234	7.95	40.0
5	0.0665	0.0333	764	28.8	1267	8.70	37.5
6	0.0700	0.0350	753	36.1	1249	9.10	40.0
7	0.0530	0.0265	904	26.9	1356	8.30	37.5
8	0.0555	0.0278	892	32.5	1337	8.19	35.0
9	0.0620	0.0310	803	31.7	1205	7.90	45.0
10	0.0630	0.0315	810	34.5	1215	8.00	42.5
11	0.0680	0.0340	761	34.6	1142	7.85	45.0
12	0.0525	0.0263	997	32.0	1319	9.20	35.0
13	0.0620	0.0310	860	32.8	1138	7.40	45.0
14	0.0620	0.0310	983	49.9	1098	9.00	55.0

TABLE VII. Correlation of the theoretical and experimental results for the transition location for the dips in Table II.

Dip #	$-h*$	$h*/b*$	R_m	Separation bubble ΔR	R_T	N_T	$F_T \times 10^6$
1	0.057	0.0285	894	37.7	1483	9.2	30
2	0.067	0.0335	831	41.6	1377	8.9	35
3	0.057	0.0285	930	39.8	1395	8.31	35
4	0.067	0.0335	807	36.5	1210	7.5	40
5	0.057	0.0285	943	41.3	1248	7.3	45
6	0.067	0.0335	855	39.0	1132	6.69	50

those of the Blasius boundary layer. Hence, the N factor increases slowly as in the case of the Blasius boundary layer until it reaches its maximum. For locations downstream of branch I of the Blasius flow, the hump appears smaller compared with the thickness of the boundary layer and hence, the separation bubble is smaller. Accordingly, the increase in the N factor in the interaction region is smaller. The end result is an overall smaller N factor. Table IV shows that the Reynolds number R_9 at which $N = 9$ does not change as the hump is moved upstream of branch I but it increases as the hump is moved downstream. We note that the first three values of R_9 appear to be identical because they were rounded to four significant figures.

C. Correlation of theoretical and experimental results

Table V shows the variations of the Reynolds number R_9 at which $N = 9$ and the computed amplification factor N_T at the experimentally measured transition location with the dimensionless frequency F for hump No. 5 in Table I. For $F = 45 \times 10^{-6}$, the maximum value of N is 8.4. It is clear that the most dangerous frequency has shifted from $F = 25 \times 10^{-6}$ for the Blasius flow to $F = 37.5 \times 10^{-6}$ for the disturbed flow. Moreover, the maximum computed amplification factor at the experimental transition location is 8.7.

The amplification of two-dimensional disturbances is the result of a complex interaction of Tollmien–Schlichting waves and shear-layer (laminar separation) instability as evident from Figs. 6 and 10. They show the variation of the streamwise velocity profile and the corresponding eigenfunction of the instability wave, respectively, with distance along the plate. Ahead of the separation region, the eigenfunction has a character typical of TS waves with two peaks, a large one at the critical layer and a small peak near the edge of the boundary layer. In the separation region, the eigenfunctions develop a third peak at the inflection point of the mean-flow profile. This peak increases with distance from the separation point, achieves a maximum that can be comparable to the peak at the critical layer, and decreases to zero at the reattachment point. The effects of the shear-layer instability are to increase the growth rates and the dangerous frequency.

Figure 11 shows the streamwise distribution of the ratio of the wavelength λ^* of the disturbance to the hump width $2b^*$. This hump is the same as that used to generate Figs. 5, 6, and 10. We note that separation starts at $x_1 = 1.03$ and ends at $x_2 = 1.15$. This ratio varies from about 0.2 before the
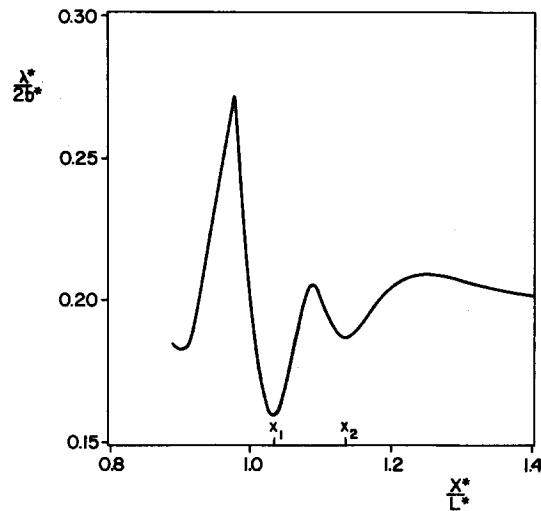
FIG. 11. Streamwise distribution of the ratio of the wavelength of the disturbance to the hump width for hump No. 14 in Table I. The flow conditions are the same as in Fig. 6; $F = 5 \times 10^{-6}$. Separation starts at $x_1 = 1.03$ and ends at $x_2 = 1.15$.

hump to a maximum of 0.27 at $x = 0.89$ and a minimum of 0.16 at $x = 1.03$. This means that the hump width is approximately five times the wavelength of the disturbance, which is consistent with the parallel flow approximation.

Tables VI and VII summarize the computed results for all the hump and dip configurations of Walker and Greening. They show the maximum (maximized over all frequencies) amplification factor N_T and its corresponding frequency at the measured transition location. The values of N_T range from 7.4 to 10, consistent with previous results for flat plates.

It is obvious that the size of the separation bubble, which is a function of the height of the hump and the Reynolds number, has a great effect on the N factor. Although a search for the most dangerous frequency has to be done, a helpful hint can be found by looking at Fig. 9 which shows that the amplification factor gets larger as the location of the hump gets closer to branch I of the stability curve of the Blasius flow. This means that the most dangerous frequency corresponds to the frequency around branch I of the Blasius flow at which $R = R_m$. But still a search has to be done.

The experimental results of dip No. 6 compared with dip No. 2 are in doubt because the dips have the same height and nearly the same Reynolds number but different measured transition lengths. Nevertheless, the correlation between the theoretical and experimental transition lengths is supportive of the e^N method.

V. CONCLUSIONS AND RECOMMENDATIONS

A. Conclusions

An analysis is conducted of the effect of imperfections consisting of humps and dips on the stability of incompressible flows over flat plates. The mean flow is calculated using interacting boundary layers. Linear quasiparallel spatial stability is used to calculate the growth rates and mode shapes of two-dimensional disturbances. Then, the amplification factor is computed. A search for the most dangerous fre-
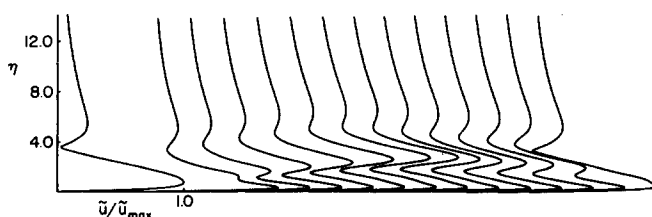

FIG. 10. The variation of the eigenfunction of hump No. 14 in Table I along the plate at frequency $F = 55 \times 10^{-6}$. The flow conditions are the same as in Fig. 6.

quency is conducted based on an amplification factor of 9 in the shortest distance. Correlations are made with the transition experiment of Walker and Greening using the e^9 method.

Based on the present investigations, we can conclude the following.

(1) The e^9 method gives a good estimate of the transition location.

(2) Increasing the size of the separation bubble, by increasing either the height-to-width ratio or the free-stream Reynolds number, causes transition to occur sooner.

(3) In the separation bubble, the calculated growth rates of the disturbances account for both the TS and shear-layer instabilities.

(4) The shape of a smooth hump or dip does not have a significant effect on the growth rates.

(5) The geometrical factors of the imperfection that govern the instability are (a) the height-to-width ratio and (b) the location of the imperfection element from the leading edge of the plate and branch I of the Blasius stability curve.

(6) The most dangerous frequency in the presence of the roughness element is not the same as that for the Blasius flow.

B. Recommendations

The present study needs to be extended by accounting for (a) nonlinear effects (in view of the large growth rates encountered in separation regions), (b) nonparallel effects, (c) the effects of concave curvature (i.e., Goertler instability), (d) the receptivity to acoustic and free-stream disturbances, and (e) the interaction between any of these instability mechanisms.

More experiments need to be conducted to provide detailed measurements of the mean profiles, mode shapes, growth rates, etc., that can be used to substantiate the theoretical results.

[1]B. J. Holmes, C. J. Obara, and L. P. Yip, NASA TP 2256, 1984.

[2]C. J. Obara and B. J. Holmes, NASA TP 2417, 1985.

[3]B. J. Holmes, C. J. Obara, G. L. Martin, and C. S. Dormack, NASA CP 2413, 1986.

[4]A. Fage, British Aeronautical Research Council 2120, 1943.

[5]M. E. Goldstein, J. Fluid Mech. **154**, 509 (1985).

[6]W. S. Walker and J. R. Greening, British Aeronautical Research Council 5950, 1942.

[7]G. S. Hislop, British Aeronautical Research Council 6443, 1943.

[8]W. S. Walker and R. J. Cox, British Aeronautical Research Council 6126, 1942.

[9]P. S. Klebanoff and K. P. Tidstrom, Phys. Fluids **15**, 1173 (1972).

[10]C. Gleyzes, J. Cousteix, and J. L. Bonnet, in *Second Symposium on Numerical and Physical Aspects of Aerodynamic Flows* (Springer, Berlin, 1983), p. 12.

[11]V. N. Vatsa and J. E. Carter, AIAA J. **22**, 1697 (1984).

[12]R. T. Davis and J. E. Carter, AIAA J. **24**, 850 (1986).

[13]R. T. Davis, J. E. Carter, and E. Reshotko, AIAA J. **25**, 421 (1987).

[14]H. P. Horton, Ph.D. thesis, University of London, Queen Mary College, 1968.

[15]R. T. Davis and M. J. Werle, in *Numerical and Physical Aspects of Aerodynamic Flows*, edited by T. Cebeci (Springer, Berlin, 1982), p. 187.

[16]S. A. Ragab and A. H. Nayfeh, in *Numerical and Physical Aspects of Aerodynamic Flows*, edited by T. Cebeci (Springer, Berlin, 1982), p. 237.

[17]M. Van Dyke, *Perturbation Methods in Fluid Mechanics* (Parabolic, Stanford, 1975).

[18]A. E. P. Veldman, AIAA J. **19**, 79 (1981).

[19]F. T. Smith, Proc. R. Soc. London Ser. A **336**, 91 (1979).

[20]A. H. Nayfeh, *Perturbation Methods* (Wiley, New York, 1973).

[21]A. H. Nayfeh, *Introduction to Perturbation Techniques* (Wiley, New York, 1981).

[22]R. R. Scott and H. A. Watts, SIAM J. Numer. Anal. **14**, 40 (1977).

[23]F. T. Smith, J. Fluid Mech. **57**, 803 (1973).

[24]A. H. Nayfeh and S. A. Ragab, AIAA Paper No. 87-0045, 1987.